Author version

Published as:

Ruh, M. L., & Hwang, J. T. (2021). Robust modeling and optimal design of rotors using blade element momentum theory. In AIAA AVIATION 2021 FORUM (Paper No. AIAA 2021-2598). https://doi.org/10.2514/6.2021-2598

BibTeX for this reference:

https://lsdolab.github.io/lsdo-publications/publication/ruh2021robust/

```
@inproceedings{ruh2021robust,
  author = {Marius L. Ruh and John T. Hwang},
  title = {Robust modeling and optimal design of rotors using blade element momentum
    theory},
  booktitle = {AIAA AVIATION 2021 FORUM},
  year = {2021},
  doi = {10.2514/6.2021-2598},
  url = {https://doi.org/10.2514/6.2021-2598}
}
```

Robust modeling and optimal design of rotors using blade element momentum theory

Marius L. Ruh* and John T. Hwang†
University of California San Diego, La Jolla, CA, 92093

In aircraft conceptual design, a fast and robust model for rotor aerodynamic analysis is valuable. A commonly used method is blade element momentum (BEM) theory, which combines momentum theory and blade element theory to predict rotor performance based on given blade airfoil and rotor planform geometry, the latter of which is not always available. In this paper, we present new theory and numerical results that advance BEM methods through four contributions. First, we present a unified formulation of the BEM equations that avoids singularities in conditions with both zero and non-zero normal inflow velocity. Second, we present a theorem that states the conditions under which the root-finding algorithm in the BEM method is guaranteed to converge. We explain that these conditions are satisfied in nearly all scenarios, and in fact, the algorithm converged successfully in all cases in a large set of numerical experiments. Third, we provide a new interpretation of the commonly used figure of merit metric as the product of component efficiencies considering rotational momentum and blade profile drag losses. Finally, we present a new blade design method based on BEM theory that uses an ideal-loading assumption. This method only requires chord and airfoil information at a single location along the span of the blade. This method also back-computes the twist and chord distributions, thereby providing the optimal rotor shape. Such a method is expected to be particularly useful in an aircraft sizing context, in which the performance of an optimal rotor can be easily evaluated without solving a separate optimization problem. Collectively, this set of contributions is expected to facilitate the use of BEM models in multidisciplinary design optimization algorithms for the design of electric aircraft.

I. Introduction

Early stages of aircraft design often make use of blade element momentum (BEM) theory to model and size the rotors. One advantage of BEM is that it can take into account blade airfoil polars and the radial twist and chord profiles. However, this type of information is not always available, which can make high level rotor sizing difficult. By contrast, general momentum theory only requires the rotor diameter as a model input, making it easier to obtain initial rotor sizing estimates if the detailed rotor geometry is unknown. However, it is less accurate than BEM theory.

General momentum theory and blade element momentum theory are high-level estimations of the performance of a rotor which, due to their computationally efficient nature, are commonly used in the early stages of the design process, including in multidisciplinary design optimization (MDO) algorithms. One MDO tool that has been gaining wider use in the last two years is NASA's OpenMDAO framework, which uses gradient-based optimization algorithms to solve coupled systems in a computationally efficient manner [1]. Both general momentum theory and BEM theory have already been implemented in OpenMDAO and used to solve large-scale optimization problems [2]. While general momentum theory and BEM individually provide certain benefits, there is a need for a convenient and easy-to-use design tool that models rotor performance efficiently and facilitates the initial design and sizing of rotors. Such a tool will be particularly useful in the design of electric aircraft for the emerging sector of urban air mobility (UAM).

In this paper, we aim to present new theory and numerical results that advance blade element momentum theory methods. To achieve this goal we need to meet four objectives. First, we unify BEM equations in a way that avoids singularities and works for zero and non-zero normal inflow velocity. Second, we introduce a theorem that states the conditions for which a bracketed search root finding algorithm crucial to BEM is guaranteed to converge. Third, we demonstrate a new interpretation of the commonly used figure of merit, showing that it represents aerodynamic losses due to blade profile drag and rotational induced losses. Fourth, we present a new ideal-loading design method that requires information regarding the chord length and airfoil polar at only one section along the rotor blade. In meeting

*MS student, Mechanical and Aerospace Engineering, AIAA Member
†Assistant Professor, Mechanical and Aerospace Engineering

these objectives we aim at developing a high level rotor design tool that expands on the capabilities of BEM methods and facilitates rotor analysis in a MDO setting.

In the following sections we first present a succinct literature survey of research efforts that have been centered around general momentum theory as well as blade element momentum theory. In section III, we provide a modernized review of classical BEM. Afterwards, we present two modifications to BEM methods in section IV. Next, we explain the theory behind our new ideal-loading design method in section V, starting with the derivation of the ideal-loading condition that lies at the heart of the analysis and finishing with the back-computation of the ideal rotor shape. Lastly, we present the results of our work in section VI through validation plots and parameter sweeps that provide valuable insight for rotor design.

II. Literature Survey

Since general momentum and BEM theory are well established, they have been the study of many publications investigating high level propulsion models for rotor driven aircraft. Ohad Gur [3] used momentum theory to estimate the maximum propulsive efficiency as well as the maximum available thrust and found that general momentum theory provides an accurate and computationally efficient estimation for the propulsion model early in the design process. Gur and Rosen [4–6] also investigated variations of blade element and momentum theory. In [5] the main three types of models under investigation were momentum models, lifting line models and vortex models. Results showed that in steady level flight, where the inflow is perpendicular to the rotor disc, the differences between the models is negligible, underlining the effectiveness of blade element momentum theory and general momentum theory. One major limitation of BEM theory and general momentum theory is its diminishing accuracy at low advance ratios, which Gur and Rosen investigated in [4], proposing a simple correction to BEM theory to account for slow operating conditions.

Madsen et al. [7] also validated blade element momentum theory based on comparisons with actuator disk simulations. They found that blade element momentum theory overestimates the induced velocities near the rotor hub as it neglects the pressure in the wake due to rotational effects. Conversely, BEM theory underestimated the induced velocities near the rotor tip when compared to actuator disk simulations. Madsen et al. also published a separate paper [8], investigating the shortcomings of blade element momentum theory based on analytical and numerical results. They confirmed the observation of under-and overestimation of the induction near the rotor hub and tip and proposed a modified version of BEM theory that addresses this shortcoming. Other noteworthy and insightful studies of blade element momentum theory can be found in [9–13].

Axial momentum theory, a simplified form of general momentum theory, has been validated by Bontempo and Manna in [14] through a CFD approach. They also investigated the shortcomings of axial and general momentum theory in [14, 15] and evaluated the effects of two main errors in the formulation of momentum theory, which stem from the use of the differential form of the axial momentum theory and the linearization of the tangential velocity terms. Comparing the effects of these errors to a semianalytical actuator disk model, Bontempo and Manna reached a similar conclusion to Madsen et al, observing that axial momentum theory overestimates the axial induced velocity in the tip and hub regions. Thus, both, general momentum theory and blade element momentum theory lead to a miscalculation of the induced velocities near the rotor hub and tip. Moreover, Bontempo and Manna showed that due to the assumptions made in axial momentum theory significant error is introduced to the model as the rotor load is increased.

Several efforts have been made to improve upon blade element momentum theory and address some of its shortcomings. Whitmore and Merrill [16] addressed the assumption made in BEM theory that the local angle of attack is small at all sections along the blade, which has been shown to be inaccurate at high advance ratios. They propose a nonlinear, numerical approach that better corresponds to measured rotor data. Another attempt at improving BEM theory has been made by Rwigema [17] who coupled blade element momentum theory with a vortex wake representation of the slipstream to model the relationship between the vorticity distribution throughout the slipstream and the propeller forces. McCrink and Gregory [18] also based their analysis of small UAS electric aircraft around blade element momentum theory and focused on adjusting the model to account for tip losses, Mach effects, three-dimensional flow components and Reynolds scaling. They were able to validate the modifications made to the blade element momentum model through experimental results. Modifying the BEM equations to account for hub and tip losses has been researched extensively and the following references explore multiple approaches with varying levels of fidelity: [19–22].

III. Review of classical blade element momentum theory

This section is a review of classical blade element momentum (BEM) theory, which combines momentum theory and blade element theory, two different approaches to low-fidelity rotor aerodynamic modeling. A thorough derivation of both theories was first presented by Glauert in the 1930s [23]. Since then, BEM theory has been extensively investigated and its computational efficiency and physical accuracy make it a powerful tool for initial rotor sizing and analysis. In the subsequent section we aim to present a modernized form of the BEM equations in a concise and easy-to-digest manner. This particular form of the BEM equations is advantageous since it works under zero and non-zero normal inflow velocities. Conventional implementations do not work under zero inflow conditions due to the use of normalized induction factors to represent the effect of rotor induced velocities. These induction factors introduce a singularity when there is zero normal inflow velocity. We circumvent this problem by developing the equations in terms of non-normalized variables.

A. Nomenclature

To facilitate the understanding of the subsequent analysis we illustrate the geometric interpretation of BEM in Fig 1, separated into momentum (a) and blade element (b) theory. We also present important variables and parameters in table 1 organized into three categories. Flow variables include quantities associated with the flow velocity in the axial and tangential direction. Geometric variables describe the geometry of the rotor and the streamtube while performance parameters present metrics commonly used to measure rotor performance. The subscript zero refers to the location far upstream of the rotor disk while the prime superscript refers the ultimate wake of the flow.

Table 1 Summary of variables

Flow variables		Geometric variables		Performance parameters	
V_x	axial free-stream velocity	R	rotor radius	T, C_T	thrust, coefficient
u_x	axial induced velocity at disk	r	radial distance	Q, C_Q	torque, coefficient
u'_x	axial induced velocity in wake	S_0	area of streamtube upstream	P, C_P	power, coefficient
V_θ	rotational rotor velocity	S	area swept by rotor	J	advance ratio
u_θ	rotational induced velocity at disk	S'	area of streamtube in wake	η	total efficiency
u'_θ	rotational induced velocity in wake	θ	twist angle	η_1	axial efficiency
W	resultant inflow velocity	α	angle of attack	η_2	rotational efficiency
Ω	rotational rotor speed (rad/s)	ϕ	inflow angle	η_3	profile drag efficiency
ω	rotational wake speed (rad/s)	c	chord length	FM	figure of merit
a_x	axial induction factor	σ	blade solidity	C_T/σ	blade loading coefficient
a_θ	tangential induction factor				

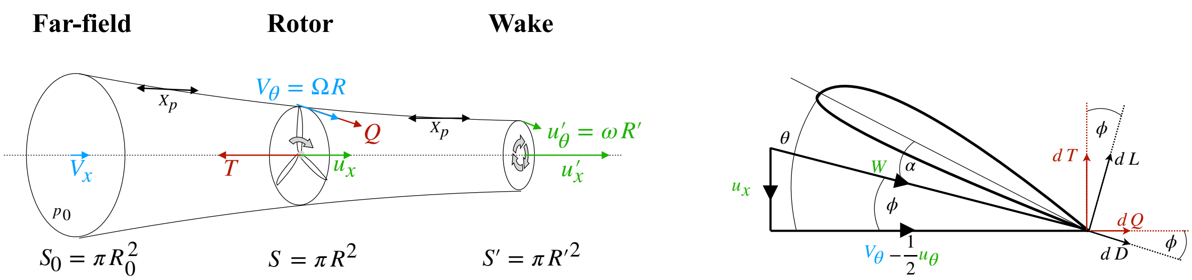

(a) Streamtube diagram for momentum theory (b) Blade element analysis

Fig. 1 Geometry for blade element momentum theory

B. Momentum Theory

Momentum theory aims to predict the performance of a rotor by analyzing how the momentum of the air changes is it passes through the rotor disc. We assume that the effect of the rotor on the air is confined to a control volume, which we call streamtube. This approach does not consider the rotor geometry and models the effect of a rotor solely based on how much momentum it imparts onto the air. In the following two subsections, we examine how this increase in momentum occurs in the axial and tangential direction of the streamtube.

1. Axial Momentum Balance

In this section we determine how the increase in momentum of the airflow in the axial direction produces thrust. To do so we consider the flow at the edges of the streamtube. Far upstream, the flow is unperturbed and has velocity V_x. As the air enters the streamtube, the effect of the pressure difference generated across the rotor disk accelerates the flow in the axial direction to a velocity of u_x at the rotor disc, and further to u'_x in the ultimate wake. Thus, by Newton's second law the increase in axial momentum per unit time produces a thrust force of

$$T = \dot{m}_{air}\left(u'_x - V_x\right) = \rho u_x S\left(u'_x - V_x\right), \tag{1}$$

where the mass flow rate $\dot{m}_{air}$ can be taken through any cross-section of the streamtube. We derived (1) based on physical intuition and a basic understanding of Newton's second law. However, we need to proceed more critically to establish the validity of the axial momentum balance through simple fluid mechanics concepts. Based on the preceding analysis as well as Fig. 1a we can write the axial momentum equation in integral form by considering the mass flux through the ends of the streamtube as well as the lateral forces acting on it. Neglecting body forces, we present the momentum equation as

$$T - X_p + p_0\left(S_0 - S'\right) = \int 2\pi\rho u_x\left(u'_x - V_x\right) r\, dr, \tag{2}$$

where r is the radial distance from the streamtube centerline and dr is the corresponding differential element. In addition, $p_0\left(S_0 - S'\right)$ is the pressure force acting on the ends of the stream tube and X_p is the lateral pressure force on the boundaries of the streamtube. It can be shown that the lateral pressure force and the pressure difference acting on the ends of the streamtube cancel each other out and, thus, we verify the result that the thrust generated by a rotor due to the increase in axial momentum can be written as

$$T = \int 2\pi\rho u_x\left(u'_x - V_x\right) r\, dr. \tag{3}$$

However, this result does not extend to an infinitesimally small thrust element dT and replacing the integral form with a differential equation in the following manner is not a proven step:

$$dT = 2\pi\rho u_x\left(u'_x - V_x\right) r\, dr. \tag{4}$$

In fact, Glauert first acknowledged [23] that (4) may introduce some error as it assumes that there is no interaction between individual annular elements. Numerous investigations [4, 14, 15, 24, 25] have shown through experiments as well actuator disk and CFD simulations that the error introduced by the differential form of the axial momentum equation is only significant for annular elements and (4) still predicts thrust accurately for the rotor as a whole when summing the individual thrust elements.

We now derive the relationship between the far-field velocity V_x, the velocity at the rotor disk u_x as well as the ultimate wake velocity u'_x. This is important since in (4) we would like to reduce the number of unknowns from u'_x and u_x to just u_x. First, the power absorbed by the rotor must equal the increase in kinetic energy of the slipstream per unit time, which leads to

$$P = \frac{1}{2}\dot{m}_{air}\left({u'_x}^2 - V_x^2\right) = \frac{1}{2}\dot{m}_{air}\left(u'_x - V_x\right)\left(u'_x + V_x\right) = \frac{1}{2}\left(u'_x + V_x\right)T. \tag{5}$$

It should be noted that in computing this increase in kinetic energy per unit time we neglect the effect of rotational induced motion in the slipstream. The power absorbed by the slipstream must also be equal to the useful work done by the thrust on the air per unit time, $\dot{W}_T$, which we express as

$$\dot{W}_T = T u_x. \tag{6}$$

Equating (5) and (6) leads to the well known result of axial momentum theory, stating that the axial induced velocity at the rotor disk u_x is equal to the arithmetic mean of the far-field velocity V_x and the maximum induced velocity in the ultimate wake u'_x:

$$u_x = \frac{1}{2}\left(u'_x + V_x\right). \tag{7}$$

In the literature, this result is commonly represented in terms of the normalized induction factor a_x as

$$u_x = V_x\left(1 + a_x\right). \tag{8}$$

More generally, this result is not true when including the effect of rotational induced velocities, causing u_x to exceed the mean of u'_x and V_x. However, in practice this effect is negligible, allowing us to use (7) to arrive the final differential form of the thrust equation:

$$dT = 4\pi\rho u_x\left(u_x - V_x\right) r\, dr. \tag{9}$$

Alternatively, using (8), we can rewrite the equation as

$$dT = 4\pi\rho V_x^2\left(1 + a_x\right) a_x r\, dr. \tag{10}$$

It is clear that (10) does not work under zero inflow conditions, meaning when V_x equals zero, because by rearranging (8) we see that a_x is undefined in that case. This is not the case with (9), making it a more robust version of the thrust equation. Lastly, we employ axial momentum theory to predict the efficiency of a rotor. Generally, we measure efficiency η as the useful output power divided by the input power:

$$\eta = \frac{P_{out}}{P_{in}}. \tag{11}$$

Here, the output power is the thrust T multiplied with the velocity at which the rotor travels in the axial direction V_x and the input power is given by (5). However, as discussed earlier, this input power does not take into account the aerodynamic losses due to rotational motion. Therefore, the following definition of efficiency is idealized as it only takes into account the axial losses, which we indicate by the notation η_1 as

$$\eta_1 = \frac{V_x T}{P} = \frac{V_x}{u_x}. \tag{12}$$

2. Angular Momentum Balance

Now, we consider the effect of aerodynamic losses due to the rotational motion in the propeller slipstream, which we neglected in the previous analysis. This happens due to the interaction of the rotor blades with the air molecules, increasing the angular momentum of the air. Treating the air molecules as point masses, the angular momentum of the air increases from zero ahead of the rotor to

$$L = u_\theta m r^2, \tag{13}$$

at the rotor disc. By conservation of angular momentum we can relate the tangential induced velocities at the rotor disk and in the ultimate wake by

$$u_\theta r^2 = u'_\theta r'^2. \tag{14}$$

This allows to write the required torque as the increase in angular momentum per unit time corresponding to an annular element. Therefore, we establish the equation for annular torque as

$$dQ = \dot{m} u_\theta r^2 = 2\pi\rho u_x u_\theta r^2 dr. \tag{15}$$

In the literature this result is often expressed in terms of the tangential induction factor a_θ, defined by Glauert [23] as $a_\theta = u_\theta / 2V_\theta$. In combination with (7), (15) then takes the following form:

$$dQ = 4\pi\rho V_x V_\theta\left(1 + a_x\right) a_\theta r^2\, dr. \tag{16}$$

Again, we observe that this result does not work for zero inflow conditions. Now, we derive a second, albeit inaccurate form of the thrust equation. We apply Bernoulli's principle to the flow immediately before and after the rotor, assuming the flow to be inviscid and incompressible. After some algebra this allows us to express the increase in pressure across the rotor disk as

$$\delta p = \rho \left(V_\theta - \frac{1}{2} u_\theta \right) u_\theta. \tag{17}$$

We use this result to establish the second, equation for thrust by applying (17) to an annular element of the rotor disk, resulting in

$$dT^* = 2\pi \delta p \, dr = 2\pi\rho \left(V_\theta - \frac{1}{2} u_\theta \right) u_\theta r \, dr. \tag{18}$$

This approach to modeling thrust is different to that taken in axial momentum theory because here we analyze the pressure jump across the rotor disk based on inviscid and incompressible flow theory. Since we neglect the effect blade profile drag (9) and (18) are not equal. However, we can use (18) to derive an expression for efficiency that captures only the effects of axial and rotational induced velocities. As a result of establishing an equation for torque via (15), we can now express the input power as the torque per unit time $dQ\Omega$ required to produce the useful thrust dTV_x. Integrating (15) and (18) we can write efficiency as

$$\eta_1 \eta_2 = \frac{V_x T^*}{\Omega Q} = \frac{V_x \pi \rho \left(V_\theta - u_\theta \right) u_\theta R^2}{\Omega \pi \rho u_x u_\theta R^3} = \frac{V_x \left(V_\theta - {}^1\!/_2 u_\theta \right)}{u_x V_\theta}. \tag{19}$$

Comparing the ideal efficiency derived from axial momentum theory via (12) with (19), we see that the loss of efficiency due to rotational induced motion only can be written as

$$\eta_2 = \frac{V_\theta - {}^1\!/_2 u_\theta}{V_\theta}. \tag{20}$$

C. Blade element theory

Blade element theory is the alternative approach to low-fidelity rotor modelling, where we consider the rotor geometry instead of the momentum of the air. In blade element theory we discretize the rotor blade radially, treating each blade element as an infinitesimally thin 2-D airfoil shown in Fig. 1b. The primary forces acting on the airfoil are lift and drag, which depend on the magnitude of the inflow velocity W, commonly represented by the non-dimensional Reynolds number, and the angle of attack α. Consequently, we need to establish the following relationships:

$$C_l = C_l \left(\alpha, Re \right) \tag{21a}$$

$$C_d = C_d \left(\alpha, Re \right). \tag{21b}$$

There are different approaches to establishing these relationships. Analytic methods commonly model C_l and C_d as linear and quadratic functions of α, respectively. However, these methods are not always accurate, particularly for C_d, and fail to model the effect of Reynolds number appropriately. This is why in our implementation we use a surrogate modelling technique called regularized minimal-energy tensor-product splines (RMTS) [26, 27] that was developed for low-dimensional problems with large datasets and quick prediction times.

To generate the dataset, we use Xfoil [28] to predict lift and drag coefficients at various combinations of α and Reynolds number within the stall regime. To smooth the raw data we apply a linear fit for the lift coefficient and seventh order least squares regression with regularization for the drag coefficient. Next, we model the post-stall behavior by applying the Viterna method [29], which extrapolates the airfoil polar to ±90° by modelling the airfoil as a flat plate. Lastly, to guarantee a smooth transition between the pre-and post-stall regimes we apply a cubic smoothing function to the transition region such that our final expressions for C_l and C_d are smooth, piecewise functions whose form we present in Appendix VII.A.

As we are interested in computing thrust and torque of a rotor, we use the inflow geometry shown in Fig. 1b to break down lift and drag into thrust and torque, leading to

$$dT = dL \cos\phi - dD \sin\phi, \tag{22a}$$

$$dQ = dL \sin\phi + dD \cos\phi. \tag{22b}$$

Next, we rewrite the differential lift and drag elements in terms of the 2-D lift and drag coefficients

$$dL = \frac{1}{2} \rho W^2 C_l c dr, \tag{23a}$$

$$dD = \frac{1}{2}\rho W^2 C_d c dr, \tag{23b}$$

where, c is the airfoil chord length and W is the resultant inflow velocity given by

$$W = \sqrt{u_x^2 + \left(V_\theta - \frac{1}{2}u_\theta\right)^2}. \tag{24}$$

This expression includes the effects aerodynamic losses due to axial and rotational induced velocities introduced in section III.B. Neglecting any losses in (24), the axial induced velocity u_x would be equal to free stream velocity V_x and the rotational induced velocity u_θ would be zero. We substitute (24) and (23) into (22) to arrive at the final form of the blade element equations given as

$$dT = \frac{1}{2}C_x \rho W^2 B c dr, \tag{25}$$

$$dQ = \frac{1}{2}C_\theta \rho W^2 B c r dr, \tag{26}$$

where C_x and C_θ are given by the following matrix equation:

$$\begin{bmatrix} C_x \\ C_\theta \end{bmatrix} = \begin{bmatrix} \cos\phi & -\sin\phi \\ \sin\phi & \cos\phi \end{bmatrix} \begin{bmatrix} C_l \\ C_d \end{bmatrix}. \tag{27}$$

D. Blade element momentum theory

In this section we explain how the results of blade element and momentum theory are combined, solving a coupled system of equations to compute thrust and torque. We start by equating the expressions for thrust (i.e. (9), (25)) and torque (i.e. (15), (26)) derived from momentum and blade element theory, leading to

$$4\pi\rho u_x (u_x - V_x)\, r\, dr = dT = \frac{1}{2}C_x \rho W^2 B c dr, \tag{28}$$

$$2\pi\rho u_x u_\theta r^2 dr = \frac{1}{2}C_\theta \rho W^2 B c r dr, \tag{29}$$

where W given by (24). After some algebra we express the induced velocities as

$$u_\theta = \frac{2\sigma C_\theta V_\theta}{4\sin\phi\cos\phi + \sigma C_\theta}, \tag{30}$$

$$u_x = Vx + \frac{\sigma C_x V_\theta}{4\sin\phi\cos\phi + \sigma C_\theta}, \tag{31}$$

where σ is the blade solidity given as

$$\sigma = \frac{Bc}{2\pi r}, \tag{32}$$

for a rotor with B blades. We note that this definition of blade solidity is a mathematical one that applies for an individual blade section. More generally, blade solidity for an entire rotor is defined by the ratio of the area of the rotor blades to the disk area swept by the rotor, which can be formally expressed as

$$\sigma_r = \frac{B\int_0^R c(r)dr}{\pi R^2}. \tag{33}$$

There are different ways of writing (30) and (31) and in the literature they are usually expressed in terms of the non-dimensional induction factors a_x and a_θ. One such formulation is given by Hwang and Ning [2] as follows:

$$a_x = \frac{C_x\sigma}{4\sin^2\phi - C_x\sigma}, \tag{34}$$

$$a_\theta = \frac{C_\theta\sigma}{2\sin 2\phi + C_\theta\sigma}. \tag{35}$$

The goal now is to derive an equation that allows us to solve for the inflow angle ϕ. To do so we use Fig. 1b to write ϕ in terms of the induced velocities as

$$\tan\phi = \frac{u_x}{V_\theta - {}^1\!/{}_2 u_\theta}. \tag{36}$$

Next, we substitute (30) and (31) into (36) and rearrange to obtain the following residual function:

$$R(\phi) = \frac{J}{\pi}\left(\sigma C_\theta + 4\sin\phi\cos\phi\right) + \left(\sigma C_x - 4\sin^2\phi\right). \tag{37}$$

In order to solve (37) for ϕ, we need to know how the chord length c as well as the local twist angle θ vary along the blade. This is because C_l and C_d depend on the angle of attack α, which we can express as $\alpha = \theta - \phi$, according to Fig. 1b. In addition, we also require knowledge of the lift and drag polar as explained in section III.C. Assuming that we know these pieces of information, we can now solve (37) via a bracketed search algorithm to determine ϕ. Then, we use (30) and (31) to find the induced velocities, which allows us to use either the blade element or the momentum equations to compute thrust and torque.

E. Summary of equations and performance metrics

In this section we summarize the most important equations from blade element momentum theory in Table 2. In addition, we present common performance metrics that are frequently used in rotor analysis and their most general definition in Table 3.

Table 2 Summary of blade element momentum theory equations

Theory	Thrust	Torque	Notes
Axial momentum	$dT = 4\pi\rho u_x(u_x - V_x)\,r\,dr$	NA	assumes that $u_x = \frac{1}{2}\left(V_x + u'_x\right)$
Angular momentum	$dT^* = 2\pi\rho\left(V_\theta - \frac{1}{2}u_\theta\right)u_\theta r\,dr$	$dQ = 2\pi\rho u_x u_\theta r^2 dr$	dT^* neglects blade profile drag
Blade Element	$dT = \frac{1}{2}C_x\rho W^2 Bc\,dr$	$dQ = \frac{1}{2}C_\theta\rho W^2 Bcr\,dr$	Assumes known c and θ profile

Table 3 Summary of rotor performance metrics

Performance variable	Metric/Coefficient	Notes
Thrust	$C_T = \frac{T}{\rho n^2 D^4}$	n is rotational speed (rev/s), D is rotor diameter
Torque	$C_Q = \frac{T}{\rho n^2 D^5}$	
Power	$C_P = \frac{T}{\rho n^3 D^5}$	
Efficiency	Forward flight: $\eta = \frac{V_x T}{\Omega Q}$ Hover: $FM = \frac{T}{P}\sqrt{\frac{T}{2\pi R^2\rho}}$	Ω is rotational speed (rad/s) FM replaces η in hover
Disk loading	$\frac{T}{S}$	S is the rotor disk area
Blade loading	$\frac{C_T}{\sigma_r}$	σ_r is defined by (33)

IV. Additions to blade element momentum theory

A. New interpretation of figure of merit

In this section we use the results of momentum theory to establish a new interpretation of the figure of merit (FM). In the previous section we presented the formula for figure of merit in Table 3. It represents the ratio of ideal power required for a hovering rotor to the actual input power. We now aim to represent this performance metric in terms of the efficiencies via momentum theory established in sections III.B.1 and III.B.2. In order to proceed, we need to derive an equation for the efficiency loss due to blade profile drag only, which we call η_3. To do so, we assume that the equations for thrust (9) and torque (15) encapsulate all sources of aerodynamic loss and apply the general definition of efficiency established in Table 3, leading to

$$\eta = \eta_1 \eta_2 \eta_3 = \frac{4V_x \left(u_x - V_x\right)}{u_\theta V_\theta}. \tag{38}$$

In combination with the expressions for η_1 and η_2 from (12) and (20) we can solve for η_3, quantifying the aerodynamic loss due to blade profile drag as

$$\eta_3 = \frac{4u_x \left(u_x - V_x\right)}{u_\theta \left(V_\theta - u_\theta\right)}. \tag{39}$$

We can use this result to further analyze the equation for figure of merit. Using the formula for FM from Table 3 and substituting the integrated expressions for thrust (9) and torque (15), we can write

$$FM = \frac{4\left(u_x - V_x\right)}{u_\theta V_\theta} \sqrt{u_x \left(u_x - V_x\right)}. \tag{40}$$

After multiplying (40) by u_x on both sides the final result is

$$FM = \frac{4u_x \left(u_x - V_x\right)}{u_\theta V_\theta} \sqrt{1 - \eta_1} = \eta_2 \eta_3 \sqrt{1 - \eta_1}. \tag{41}$$

Thus, we show that in hover, where $\eta_1 = 0$, the figure of merit captures the effects of the rotational induced velocities, η_2 as well as the blade profile drag η_3, providing a better physical intuition for what this efficiency measure represents. *This is a useful insight because knowing what the figure of merit represents can help in understanding certain rotor design choices*. Helicopter blades, for instance, are long and slender. With this interpretation of FM we conclude that one of the reasons for this design choice is to reduce blade profile drag.

B. Conditions for guaranteed convergence

In this section we revisit the residual function that was introduced at the end of section III.D and stands at the heart of blade element momentum theory. The residual function is used to determine the inflow angle ϕ from which we determine the induced velocities u_x and u_θ and ultimately the thrust and torque. We repeat the residual function here:

$$R\left(\phi\right) = \frac{J}{\pi}\left(\sigma C_\theta + 4\sin\phi\cos\phi\right) + \left(\sigma C_x - 4\sin^2\phi\right). \tag{42}$$

This implicit equation is solved via a bracketed search algorithm that finds the roots of (42) through successively smaller intervals, also called brackets. The algorithm is based on the intermediate value theorem, which states that a continuous function has at least one root in a given interval if the signs at the end of the interval are opposite. We leverage this theorem to establish the conditions for which a bracketed search algorithm to solve (42) guarantees a solution on the interval $0 \leq \phi \leq \pi/2$. Ning [30, 31] also investigates the conditions for which a bracketed search algorithm that solves a residual function similar to (42) is guaranteed to converge.

If $\phi = 0$, $C_x = C_l$, $C_\theta = C_d$ and $\theta = \alpha$. Eq. (42) becomes

$$R(0) = \sigma C_d \left(\frac{J}{\pi} + \frac{C_l}{C_d}\right). \tag{43}$$

If $\phi = \pi/2$, $C_x = -C_d$, $C_\theta = C_l$ and $\alpha = \theta - \pi/2$. Eq. (42) becomes

$$R(\pi/2) = \sigma\left(\frac{J}{\pi}C_l - C_d\right) - 4. \tag{44}$$

If we can show that $R(0)$ and $R(\pi/2)$ always have different signs, then we have guaranteed a bracket. We can identify two conditions under which $R(0) > 0$ and $R(\pi/2) < 0$. These conditions are

$$C_l(\theta) > 0 \tag{45}$$

$$C_l(\theta - \pi/2) < 0. \tag{46}$$

Theorem: If conditions (45) and (46) are satisfied, then $\phi = 0$ and $\phi = \pi/2$ defines a bracket, and a bracketed root-finding algorithm is guaranteed to converge to a solution of (42).

Proof: If we can show that we can always find a bracket, any bracketed root-finding algorithm is guaranteed to solve (42). We will show that $\phi = 0$ and $\phi = \pi/2$ defines a valid bracket under the assumptions.

Given (45) is true, all terms in (43) are positive. Therefore, it follows trivially that $R(0) > 0$.

Given (46) is true, the first term in (44) is negative. This can be seen by observing that σ, J, π, and C_d are all positive, while C_l is negative. ■

Interpretation: Conditions (45) and (46) are satisfied in any reasonable rotor analysis problem. Pitch, θ, is in the interval $(0, \pi/2)$, and $C_l(\theta)$ is positive for any symmetric or positively-cambered airfoil, thus satisfying (45). Regarding (46), $\theta - \pi/2$ would be in the interval $(-\pi/2, 0)$, and $C_l(\theta)$ would be negative, except in extremely rare circumstances in which θ is very close to $\pi/2$ and C_l is zero at a very large, negative value of α. Thus, (46) is expected to be satisfied as well for all reasonable conditions.

V. New ideal-loading design method

In this section we present a new approach to low-fidelity rotor aerodynamic modeling that is different from classical blade element momentum theory. Instead of providing a twist and chord distribution as a model input, we only specify the chord length at an arbitrary blade section. The ideal-loading design method will then evaluate the rotor performance based on an ideal-loading assumption and back-compute the twist and chord distribution, providing the geometry of a rotor that minimizes the overall aerodynamic losses. This is a significant result as it eliminates the need to use gradient based optimization via BEM to find the optimum rotor design. In the following sections we first establish the intuition behind the ideal-loading assumption and then derive the overall model architecture. To facilitate the understanding of the ideal-loading design method, we provide a visualization of the flow of equations in the Appendix VII.B Fig. 10.

A. Derivation of ideal-loading condition

To build the intuition behind the ideal-loading model, we consider a hypothetical scenario in which we have direct control over how we distribute the thrust along the rotor blade. We choose an ideal thrust distribution that minimizes the overall energy loss incurred by the rotor. This means that the rotor is ideally loaded and that any deviation from this ideal load distribution will increase the overall energy loss. In Fig. 3 the ideal thrust distribution is represented by the solid red curve and the corresponding energy loss distribution is the solid green curve. Now, we perturb the ideal thrust distribution by the same amount dT_r everywhere along the rotor span, shown by the dashed red line. Since in this scenario we only have control over the thrust, we do not know how the additional energy loss will be distributed along the blade. What we do know, however, is that the overall energy loss will increase as we move away from the ideal operating condition and we assume some arbitrary energy loss distribution dE_r shown by the dashed green line.

Now, we want to minimize the additional energy loss while keeping the total additional thrust constant. Referring to Fig. 3, this means that the goal is to minimize the total area under the green dashed curve while maintaining the total area under the red dashed curve. Since in this thought experiment we control how we distribute the thrust, we can subtract an additional thrust element at a radial section where the associated energy loss is large and add the same thrust element at a section where the energy loss is small. In doing so we minimize the additional energy loss incurred due to the perturbation of the ideal thrust distribution. This process of redistributing the additional thrust is shown in Fig.3 where in (a) the original thrust perturbation incurs a maximum additional energy loss, $dE_{r,max}$, near the midsection of the blade and a minimum additional energy loss near the tip, $dE_{r,min}$. Therefore, we can subtract a thrust element at the midsection and add it at the tip. Repeating this process of redistributing the thrust perturbation eventually leads to (b) where the additional energy loss is smaller than in (a) while the total thrust perturbation is unchanged. This leads to the central conclusion of the ideal-loading analysis, which states that in order for the overall energy loss of a rotor to be minimized, the ratio of the energy perturbation to the corresponding thrust perturbation should be constant along the rotor blade. To the knowledge of the authors, this result was first identified by Glauert [23].

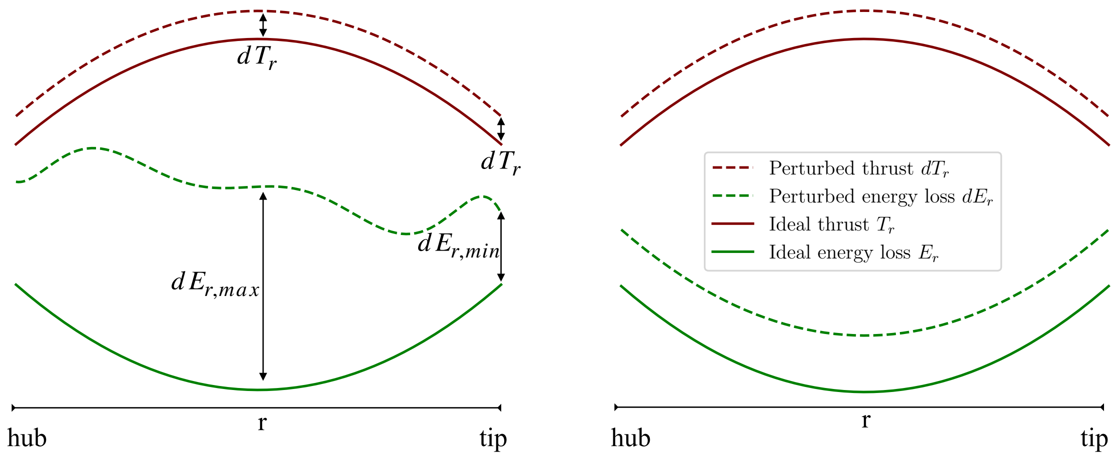

(a) Initial thrust and energy loss perturbation

(b) Redistributed thrust and energy loss perturbation

Fig. 2 Illustration of ideal-loading concept

To calculate the unperturbed energy loss E_r we first look at how it is defined in terms of input power minus output power. In general, E_r takes the following form:

$$E_r = \Omega Q_r - V_x T_r, \tag{47}$$

where $E_r = {}^{dE}/{}_{dr}$, $Q_r = {}^{dQ}/{}_{dr}$ and $T_r = {}^{dT}/{}_{dr}$. Upon substituting the expressions for thrust and torque from momentum theory via (9) and (15) the expression becomes

$$E_r = 2\pi r \rho \left(V_\theta u_x u_\theta - 2V_x u_x^2 + 2V_x^2 u_x \right). \tag{48}$$

To calculate the perturbed energy loss, we differentiate (48) with respect to the induced velocity u_x, leading to

$$\frac{dE_r}{du_x} = 2\pi r \rho \left(V_\theta u_\theta + V_\theta u_x \frac{du_\theta}{du_x} - 4V_x u_x + 2V_x^2 \right). \tag{49}$$

We differentiate with respect to u_x because the induced velocity is the source of aerodynamic loss, which determines the energy loss. In order to complete the differentiation we need to relate u_θ and u_x to form the derivative ${}^{du_\theta}/{}_{du_x}$. First, we recall the first step of the coupled solution of the BEM equations, where we equate the thrust and torque equations from momentum theory and blade element theory. This was shown in (28) and (29), which we divide by each other and apply the definition of C_x and C_θ from (27), leading to

$$\frac{2\left(u_x - V_x\right)}{u_\theta} = \frac{C_l \cos\phi - C_d \sin\phi}{C_l \sin\phi + C_d \cos\phi}. \tag{50}$$

Here we assume that we are operating under conditions that maximize the lift-to-drag ratio, such that C_d is negligibly small. Thus, the RHS of (50) becomes ${}^{1}/{}_{\tan\phi}$ to which we apply (36), relating the inflow angle ϕ to the induced velocities. This allows us to rewrite (50) as

$$2u_x\left(u_x - V_x\right) = u_\theta\left(V_\theta - {}^{1}/{}_{2}u_\theta\right), \tag{51}$$

which we can differentiate with respect to u_x, resulting in

$$\frac{du_\theta}{du_x} = \frac{2\left(2u_x - V_x\right)}{V_\theta - u_\theta}. \tag{52}$$

We substitute this expression into (49), which yields the final form of the energy loss perturbation as

$$\frac{dE_r}{du_x} = 2\pi r \rho \left(V_\theta u_\theta + V_\theta u_x \frac{2\left(2u_x - V_x\right)}{V_\theta - u_\theta} - 4V_x u_x + 2V_x^2 \right). \tag{53}$$

Next, we need to differentiate T_r with respect to u_x to capture the perturbation of thrust:

$$\frac{dT_r}{du_x} = 4\pi r\rho\left(2u_x - V_x\right). \tag{54}$$

Now, we are in a position to apply the conclusion of the ideal-loading analysis, which states that the ratio of the perturbed energy loss to the perturbed thrust must be constant along the rotor blade. Therefore we divide (53) by (54) and after some algebra we obtain the following expression:

$$\frac{V_\theta u_\theta}{2u_x - V_x} + \frac{2V_\theta u_x}{V_\theta - u_\theta} - 2V_x = S, \tag{55}$$

where we call S the ideal-loading constant.

B. Derivation of ideal-loading solution

Assuming we know S, the two unknowns in (55) are u_x and u_θ. In practice, to determine S, we apply the BEM equations once at an arbitrary section along the rotor blade where we assume some value for the chord length and a maximum lift-to-drag ratio C_l/C_d for the airfoil of our choice. This allows us to find u_x and u_θ at that blade section from which we find S. Now, the goal is to rewrite (55) in terms of a single variable that connects u_x and u_θ. This unifying variable is η_2, which we derived earlier in section III.B.2 and repeat here:

$$\eta_2 = \frac{V_\theta - 1/2\, u_\theta}{V_\theta}. \tag{56}$$

This can be rearranged to write u_θ in terms of η_2:

$$u_\theta = 2V_\theta\left(1 - \eta_2\right). \tag{57}$$

Next, we recall (50) but do not make the assumption that $C_d \approx 0$ because we want our model to capture the effect of blade profile drag. Thus, (50) becomes:

$$\frac{2\left(u_x - V_x\right)}{u_\theta} = \frac{C_l\left(V_\theta - 1/2\, u_\theta\right) - C_d u_x}{C_l u_x + C_d\left(V_\theta - 1/2\, u_\theta\right)}. \tag{58}$$

Substituting (56) into (58) and solving for u_x leads to

$$u_x = \left(\frac{V_x - V_\theta C_d/C_l}{2}\right) + \sqrt{\left(\frac{V_x - V_\theta C_d/C_l}{2}\right)^2 + \eta_2 V_\theta^2\left(1 - \eta_2 + \frac{V_x}{V_\theta}\frac{C_d}{C_l}\right)}. \tag{59}$$

Having established expressions for u_x and u_θ, we can now rewrite (55) in terms of η_2 by substituting (57) and (59). After some algebra we obtain a fourth order polynomial of the form

$$P(\eta_2) = a_4\eta_2^4 + a_3\eta_2^3 + a_2\eta_2^2 + a_1\eta_2 + a_0, \tag{60}$$

where the polynomial coefficients are in terms of V_x, V_θ, C_l, C_d and S, shown in Appendix VII.A. The roots of this quartic equation represent the local annular efficiency η_2, which can be determined at each blade section using a root finding algorithm. Even though there are four mathematical roots that can be real or complex, (57) requires that η_2 lies between 0.5 and 1 since the tangential induced velocity cannot be greater than the rotational velocity of the rotor. In practice, only one root satisfies this requirement. Once the distribution of η_2 is found, the induced velocities are calculated via (57) and (59) from which thrust and torque are easily determined from momentum theory.

C. Computation of ideal blade shape

Now that we found thrust and torque, the last step is to back-compute the chord and twist distribution. We recall from Fig. 1 that the twist angle is given as $\theta = \phi + \alpha$. Since we know how the induced velocities u_x and u_θ vary along the blade, we can use (36) to compute the inflow angle ϕ at each radial section. To determine the angle of attack, we make the assumption that α is constant along the blade such that it maximizes the lift-to-drag ratio. This is a good assumption for our model as it aligns well with the ideal-loading analysis. Knowing α and ϕ we can compute the twist angle θ. The computation of the chord is straightforward and involves rearranging either (25) or (26) to isolate chord c. For instance, we can compute c as

$$c = \frac{2dT}{C_x\rho W^2 B dr}. \tag{61}$$

VI. Results

A. Validation of blade element momentum theory

Figure 3 presents the results of a validation study for our BEM model. We use the UIUC propeller database [32], which contains wind tunnel measurements for small propellers. We choose an APC sport 10×6 propeller with a true diameter of 0.254 m and given twist and chord distribution, which we use as inputs to our BEM model. The APC manufacturer claims that their propellers use a blend of the NACA 4412, Clark-Y and Eppler E63 airfoils for the majority of their propellers*, which is the reason for the choice of airfoils in Fig. 3. We see that the output of our BEM implementation agrees with the wind tunnel results from the UIUC database.

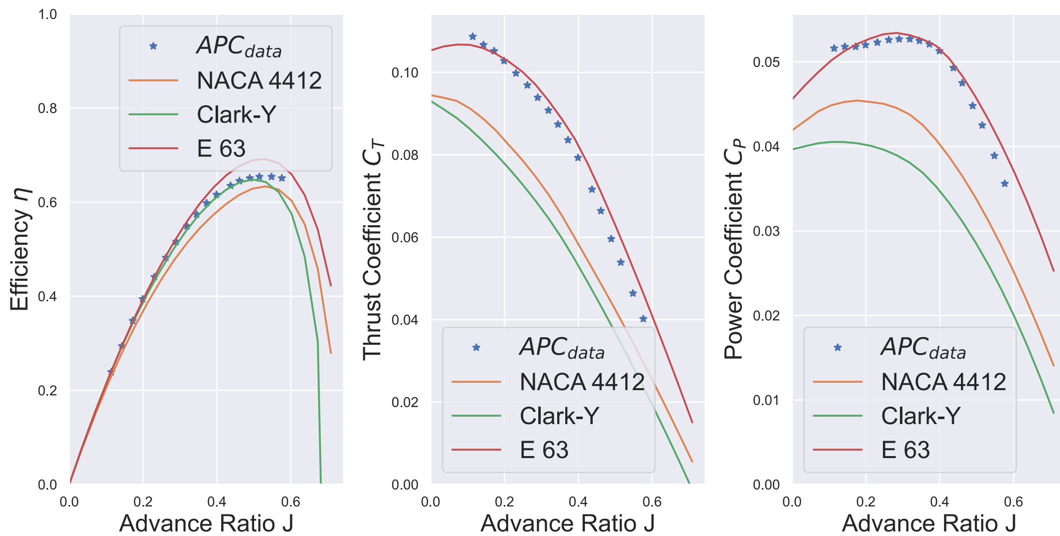

Fig. 3 Validation of BEM equations

B. Verification of ideal-loading design method

Babuska and Oden [33] split verification into code and solution verification. The former confirms that the computer code is executed faithfully while the latter assesses the numerical accuracy with which the physical model is approximated, involving a posteriori estimation of a numerical or discretization error. To verify the ideal-loading design method we use our BEM implementation to perform gradient based optimization where torque is our objective function and thrust is constrained to the output of the ideal-loading design method. The purpose of the ideal-loading design method is to predict the performance of a rotor that incurs minimum aerodynamic losses. Therefore, our choice of torque as an objective function is appropriate since minimizing torque implies minimizing the aerodynamic losses. In Fig. 4 the output of the ideal-loading design method is shown in blue and the result of the BEM optimization is shown in red. The optimization results were obtained using the SNOPT [34] algorithm.

To provide physical context behind the optimization, the thrust constraint was chosen such that the rotor produces enough thrust to support the weight of the airbus Vahana, an electric urban air mobility (UAM) concept with a mass of 725 kg and eight rotors that each have three blades and a radius of 0.75 m. These parameters were taken from two papers, investigating different aspects of UAM designs [35, 36]. Fig. 4 provides code verification of the ideal-loading design method. We see that the back-computed blade shape (i.e. the chord distribution) and twist distribution from the ideal-loading model agrees well with the BEM optimized twist and chord distribution. Also, we confirm that the assumption of a constant maximum lift-to-drag ratio made in the ideal-loading model is reasonable since the optimized lift and drag coefficient are constant for the majority of the rotor blade and only deviate at the root and hub. Most importantly, the energy loss distribution along the rotor blade from the BEM optimization and ideal-loading model agree and the difference in total energy loss between the optimization and ideal-loading output is roughly 0.01%. Assuming the BEM optimization result to be the true solution, the numerical closeness to the output of the ideal-loading design method provides solution verification. This is a significant result because it shows that the ideal-loading model predicts

*https://www.apcprop.com/technical-information/engineering/

the performance of an optimal rotor and finds its geometry with one model evaluation, eliminating the need to use gradient based optimization to achieve the same result. Not only does the ideal-loading design method save time, it is also more robust than performing optimization, which is prone to convergence failure and powerful optimizers like SNOPT are costly and not available to the public domain.

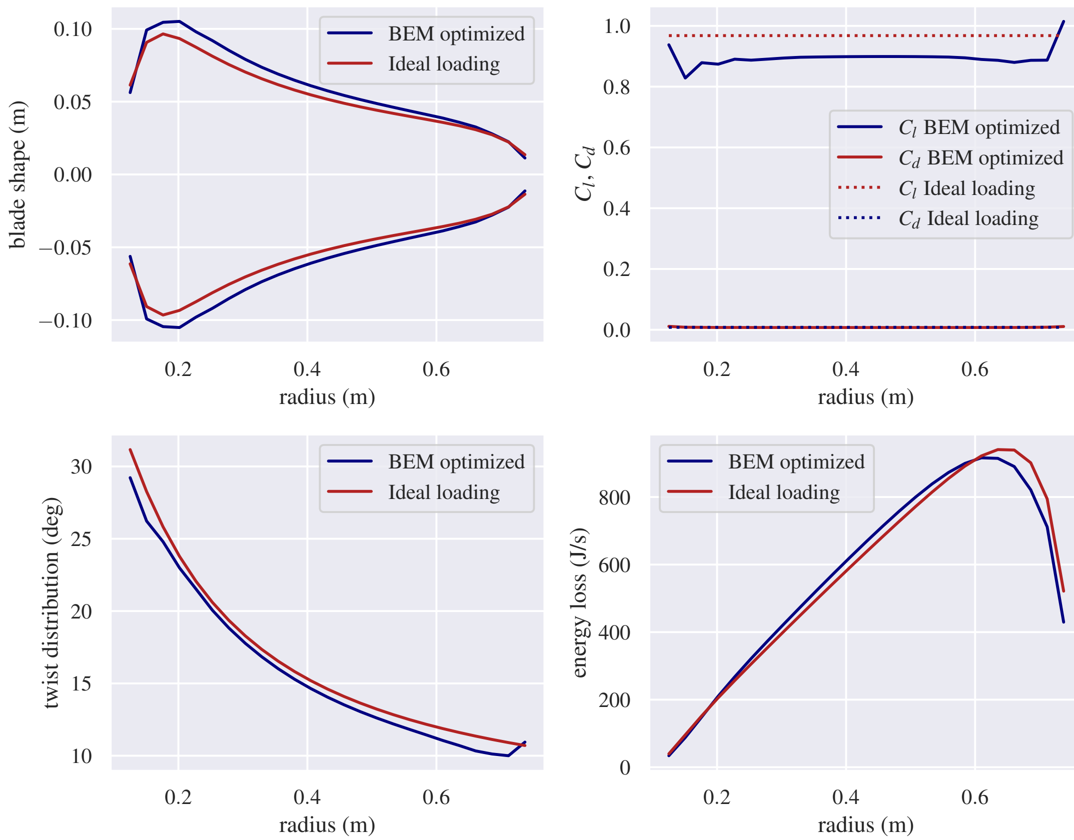

Fig. 4 Verification of ideal-loading design method

C. Mesh refinement study

In this section, we present the results of a mesh refinement study, shown in Fig. 5 using blade element momentum theory. We assume an arbitrary twist and chord distribution and vary the number of radial nodes that define the rotor mesh in the spanwise direction. In addition, we also change the operating conditions via advance ratio J, varied across the rows, as well as the blade blade solidity σ, varied via the different curves on the subplots. The goal of this study is to see how many radial nodes are required for BEM analysis to produce accurate results. Fig. 5 shows that in general, at least 25 nodes are necessary. There are no notable effects of advance ratio or blade solidity on how many radial nodes are needed. The results of this section are insightful because knowing the right mesh size is important. Although blade element momentum theory is a fast and computationally efficient model, a mesh that is too fine will unnecessarily increase the computational cost.

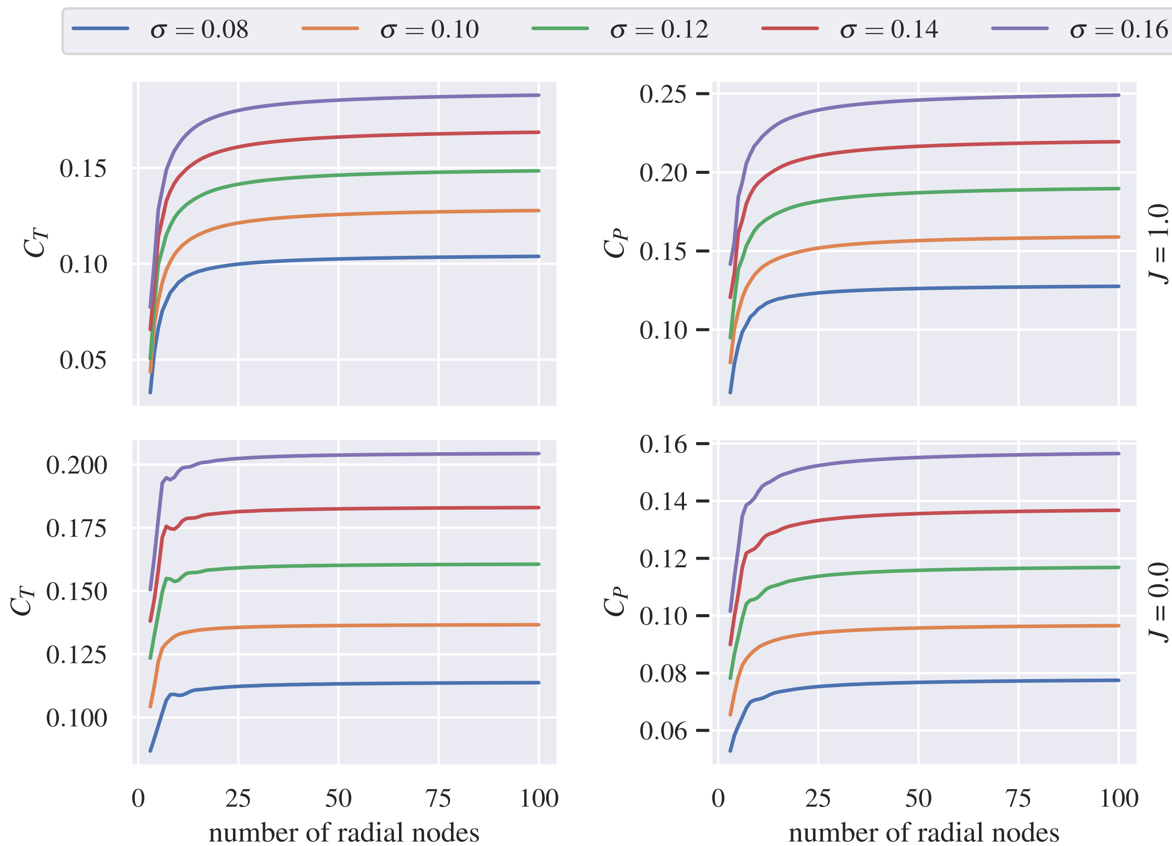

Fig. 5 BEM radial mesh refinement study at different blade solidity values σ and advance ratio J

D. Blade element momentum theory parameter sweeps

In this section, we present multiple figures showing certain parameter sweeps using the BEM model. On the y-axis we show the rotor performance metric η, while on the x-axis we vary advance ratio J. In addition, we change blade solidity σ across the columns of the subplots and use multiple curves on each subplot to change the variable blade pitch angle θ. Lastly, we use the rows of the suplots to vary the hub radius and sideslip angle. The purpose of these plots is to highlight interesting trends in commonly used rotor metrics that might be useful to rotor designers.

Before presenting the results, we explain how the BEM equations can be modified to include non-normal inflow condition such as sideslip velocity. In the derivation of blade element momentum theory (see section III), we only considered normal inflow conditions, where the free-stream velocity is perpendicular to the rotor disk and there is no sideslip velocity. Here, we show that in case of some sideslip velocity, the BEM model remains effective and only requires a minor adjustment to the model inputs. We illustrate the most general flow geometry for sisdelip analysis in Fig. 6. The rotor disk coincides with the yz-plane and the x-axis is perpendicular, coming out of the page. Furthermore, we decompose the inflow vector into x, y and z components v_x, v_y and v_z, respectively, where v_x is not necessarily the same as the free stream velocity V_x that was introduced for normal inflow condition. Now, the goal is to transform the cartesian velocities into polar velocities. The tangential or azimuthal inflow velocity will be composed of v_y, v_z and the rotational velocity of the rotor Ωr, while the axial component is simply v_x. According to the direction of velocities shown in Fig. 6, the tangential velocity at any radial section r is

$$V_\theta = v_y \sin\theta - v_z \cos\theta + \Omega r. \tag{62}$$

We see that if there is no sideslip, the tangential velocity is simply the rotational speed of the rotor like in section III. Lastly, to apply the BEM equations with sideslip, we need to discretize the rotor disk tangentially in addition to the radial discretization, which incurs a higher computational cost.

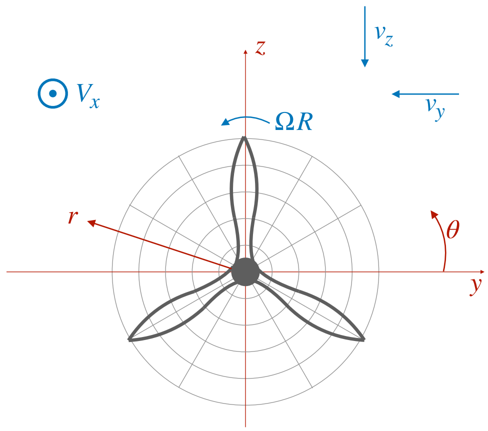

Fig. 6 Illustration of sideslip analysis

The results of the parameter sweeps provide some valuable insight into how operating conditions as well as blade geometry impact the performance of a rotor. In Fig. 7 we investigate how advance ratio J (x-axis), blade solidity σ (columns), blade pitch angle θ (curves) and hub radius (rows) affect efficiency η (y-axis). We see that higher pitch angles increase rotor efficiency at high advance ratios. In addition, larger hub-radii decrease the overall rotor efficiency. The same is true for larger values of blade solidity, although in that case the effects are less pronounced. Results from the sideslip analysis are shown in Fig. 8. To provide context, in this study we vary the angle of a sideslip velocity of 10 m/s from 0 degrees (purely lateral sideslip) to 90 degrees (perpendicular to rotor disk in the opposite direction of V_x). We see changing the sideslip angle significantly reduces the rotor efficiency. Larger pitch angles generally increase the efficiency at higher advance ratios.

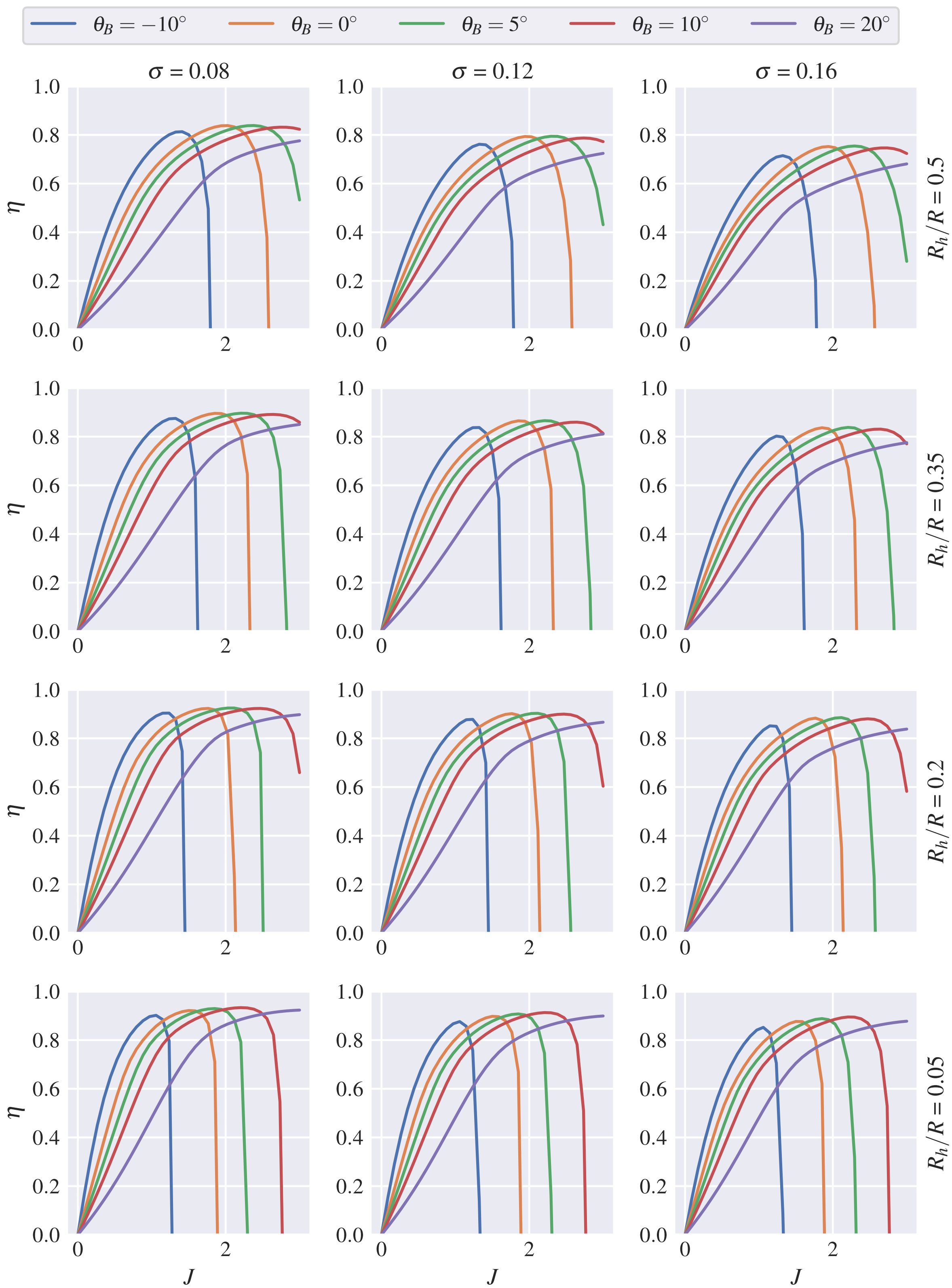

Fig. 7 BEM η parameter sweeps changing R_{hub}/R

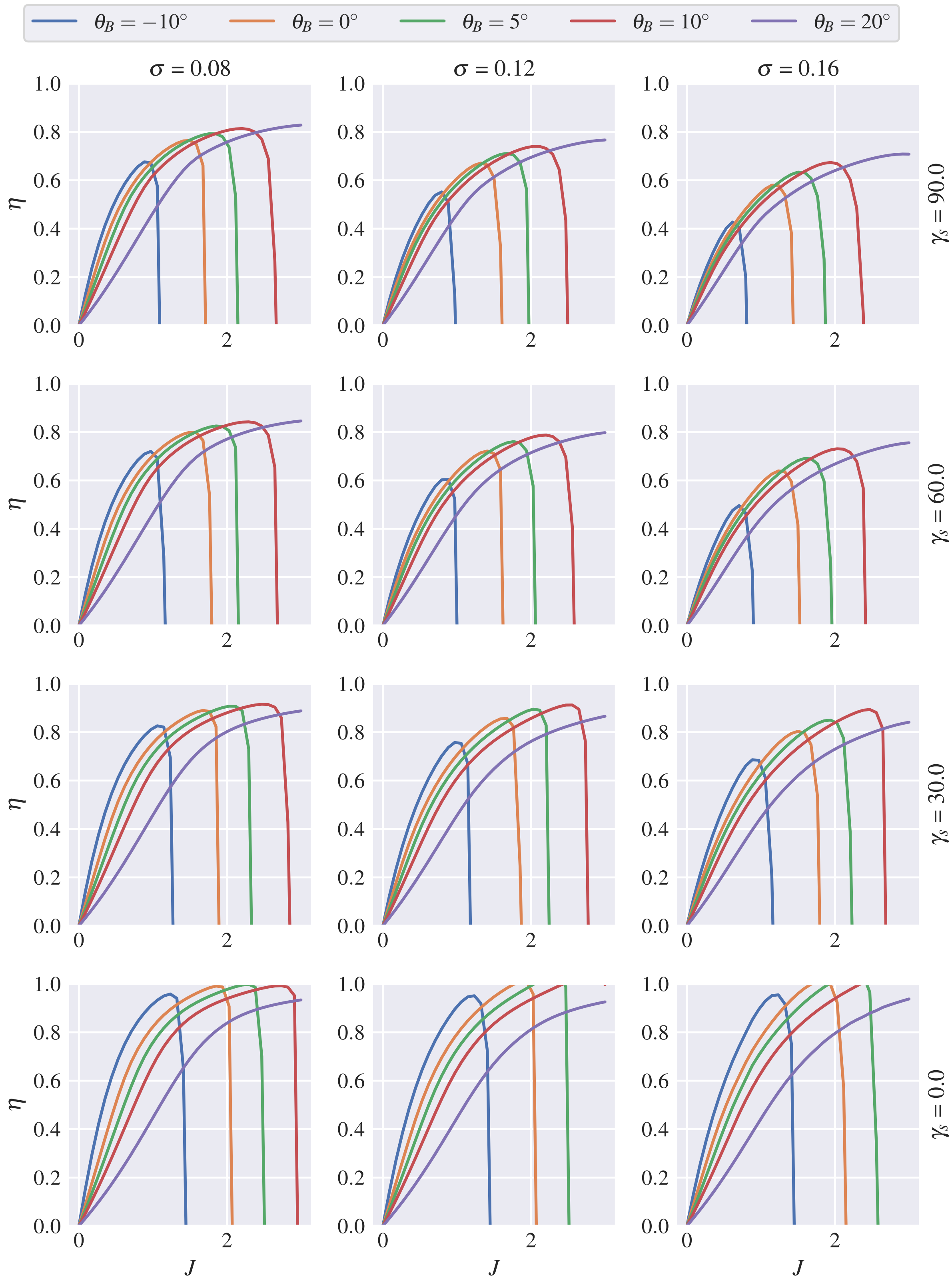

Fig. 8 BEM η parameter sweeps changing sideslip angle γ_s

E. Ideally loaded blade shapes

In this section we present results from the new ideal-loading design method. In Fig. 9 we show the effect of changing the reference chord length at an arbitrary rotor section on the back-computation of the twist and chord profile. We see that there is a significant effect on the blade shape and twist distribution as we vary the reference chord length. Choosing a small reference chord length leads to a thin and slender blade shape and a low twist distribution. The opposite is true for choosing a larger chord length.

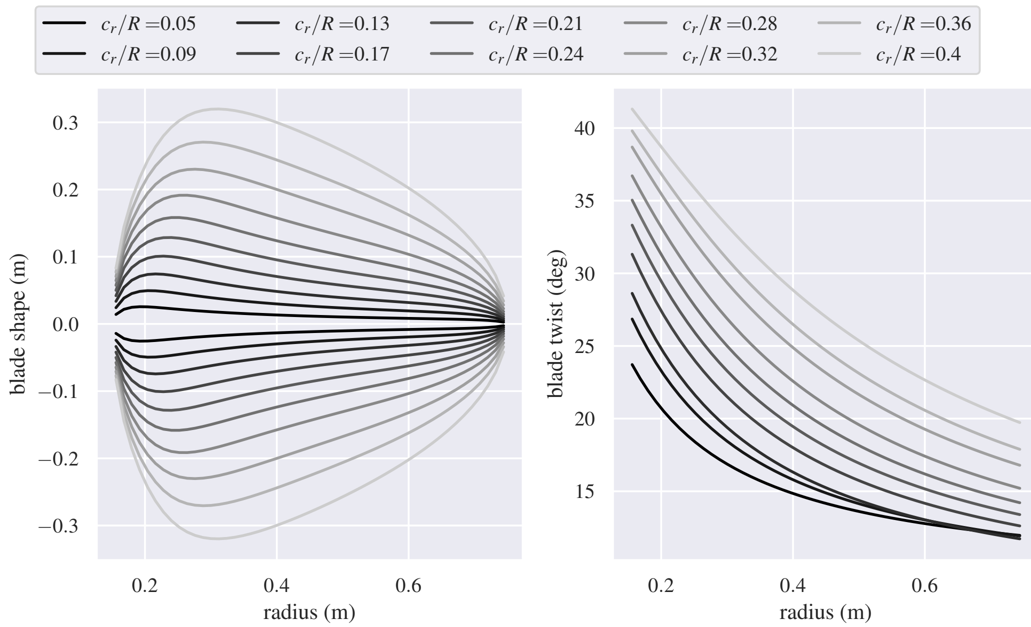

Fig. 9 Ideal-loading design method: changing reference chord length c_r at arbitrary rotor section $(0.2R)$

VII. Conclusion

In this paper we presented new theory and numerical results that advance blade element momentum theory methods. These results were made possible by achieving four milestones. First, we reviewed classical BEM theory in section III in a modernized way. We emphasized that our presentation of the BEM equations uses the induced velocities u_x and u_θ instead of the non-dimensional normalized induction factors a_x and a_θ, which avoids singularities under non-zero and zero normal inflow conditions, expanding the robustness of our implementation.

Second, in section IV.B we presented a theorem that states the conditions for which the bracketed search algorithm used in the BEM equations to find the inflow angle ϕ is guaranteed to converge. This is a crucial step without which the BEM equations cannot be solved and therefore guaranteeing convergence of the bracketed search algorithm improves the robustness of our implementation, which is important in a MDO setting where multiple disciplines are combined.

Third, we showed in section IV.A that the figure of merit can be written as the product of component efficiencies, $\eta_2\eta_3$, considering rotational momentum and blade profile drag losses. This is a useful insight as it can explain certain rotor design choices and quantifies the performance of a rotor in hover in a meaningful and intuitive way.

Fourth, in section V we presented a new blade design method that builds on BEM theory and uses an ideal-loading assumption. To start, we derived the ideal-loading condition, stating that a rotor is ideally loaded if the ratio of energy loss per unit thrust is constant along the blade. Then, we used this condition to derive equations that predict the performance of an ideal rotor. Lastly, we manipulated these equations to back-compute the geometric rotor shape. This new rotor design method allows for the quick and robust design and sizing of rotors in the early stages of the design process. It eliminates the need to perform gradient based optimization through the BEM equations in order to find the ideal rotor planform geometry since the same result is achieved with just one model evaluation of the ideal-loading design method. We anticipate that collectively, these four contributions will facilitate the use of BEM models in multidisciplinary design optimization algorithms for the design of electric aircraft.

Appendix

A. Equations
The equations for the piecewise lift and drag coefficients are as follows:

$$C_l = \begin{cases} C_{l_0} + C_{l_\alpha}\alpha, & \alpha \le \alpha_{stall} - \epsilon \\ c_3\alpha^3 + c_2\alpha^2 + c_1\alpha + c_0, & \alpha_{stall} - \epsilon \le \alpha \le \alpha_{stall} + \epsilon \\ A_1 \sin 2\alpha + A_2 \frac{\cos^2\alpha}{\sin\alpha}, & \alpha \ge \alpha_{stall} + \epsilon \end{cases} \tag{63a}$$

$$C_d = \begin{cases} a_7\alpha^7 + a_6\alpha^6 + a_5\alpha^5 + a_4\alpha^4 + a_3\alpha^3 + a_2\alpha^2 + a_1\alpha + a_0, & \alpha \le \alpha_{stall} - \epsilon \\ d_3\alpha^3 + d_2\alpha^2 + d_1\alpha + d_0, & \alpha_{stall} - \epsilon \le \alpha \le \alpha_{stall} + \epsilon \\ B_1 \sin^2\alpha + B_2 \cos\alpha, & \alpha \ge \alpha_{stall} + \epsilon \end{cases} \tag{63b}$$

where the smoothing region is confined to $\epsilon = \pm 1.5°$ and the Viterna coefficients A_1, A_2, B_1, B_2 can be found in [29].

Equation (64) repeats the quartic equation presented in section III C, including the polynomial coefficients.

$$\begin{aligned}
R(\eta_2) &= a_4{\eta_2}^4 + a_3\eta_2^3 + a_2\eta_2^2 + a_1\eta_2 + a_0, \\
&\text{where} \\
a_0 =& (V_\theta^2(2V_\theta^2 + 2V_x^2 + SV_x)(4C_d^2V_\theta^2 - 10C_dC_lV_\theta V_x - 2SC_dC_lV_\theta - 2C_l^2V_\theta^2 + 4C_l^2V_x^2 + SC_l^2V_x))/C_l^2 \\
a_1 =& (V_\theta^2(-16C_d^2SV_\theta^2V_x - 24C_d^2V_\theta^4 - 24C_d^2V_\theta^2V_x^2 + 12C_dC_lS^2V_\theta V_x + 12C_dC_lSV_\theta^3 + 68C_dC_lSV_\theta V_x^2 + \\
& 84C_dC_lV_\theta^3V_x + 84C_dC_lV_\theta V_x^3 + 4C_l^2S^2V_\theta^2 - 4C_l^2S^2V_x^2 + 24C_l^2SV_\theta^2V_x - 20C_l^2SV_x^3 + 40C_l^2V_\theta^4 + \\
& 16C_l^2V_\theta^2V_x^2 - 24C_l^2V_x^4))/C_l^2 \\
a_2 =& -(V_\theta^2(-16C_d^2SV_\theta^2V_x - 16C_d^2V_\theta^4 - 16C_d^2V_\theta^2V_x^2 + 24C_dC_lS^2V_\theta V_x + 8C_dC_lSV_\theta^3 + \\
& 112C_dC_lSV_\theta V_x^2 + 128C_dC_lV_\theta^3V_x + 128C_dC_lV_\theta V_x^3 + 20C_l^2S^2V_\theta^2 - 4C_l^2S^2V_x^2 + 104C_l^2SV_\theta^2V_x - \\
& 16C_l^2SV_x^3 + 132C_l^2V_\theta^4 + 116C_l^2V_\theta^2V_x^2 - 16C_l^2V_x^4))/C_l^2 \\
a_3 =& (16V_\theta^3(2C_lS^2V_\theta + C_dS^2V_x + 9C_lSV_\theta V_x + 4C_dSV_x^2 + 10C_lV_\theta^3 + 4C_dV_\theta^2V_x + 10C_lV_\theta V_x^2 + 4C_dV_x^3))/C_l \\
a_4 =& -16V_\theta^4(S^2 + 4SV_x + 4V_\theta^2 + 4V_x^2)
\end{aligned} \tag{64}$$

B. Figures

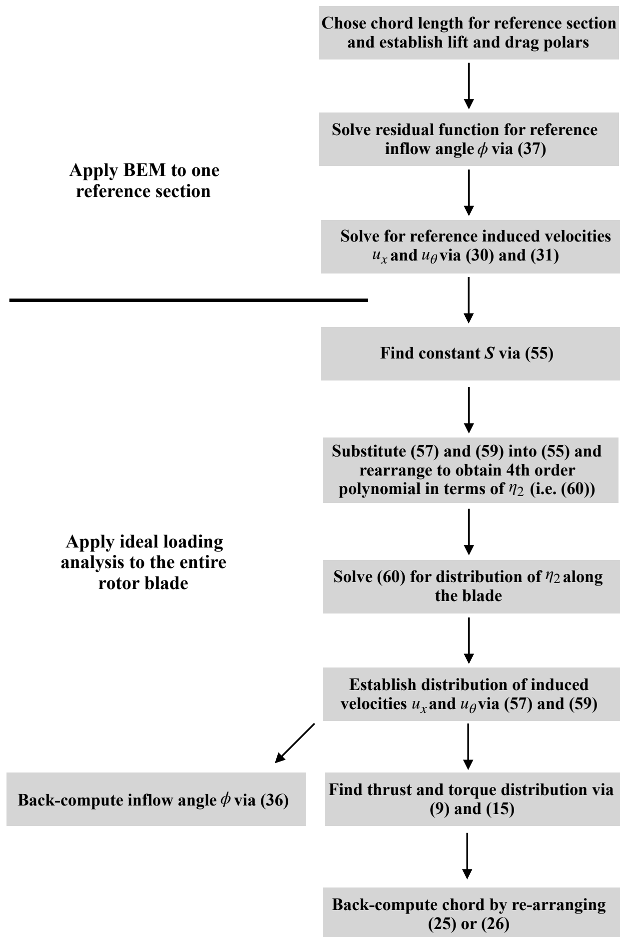

Fig. 10 Visualization of ideal-loading model architecture

References

[1] Gray, J. S., Hwang, J. T., Martins, J. R., Moore, K. T., and Naylor, B. A., "OpenMDAO: An open-source framework for multidisciplinary design, analysis, and optimization," *Structural and Multidisciplinary Optimization*, Vol. 59, No. 4, 2019, pp. 1075–1104.

[2] Hwang, J. T., and Ning, A., "Large-scale multidisciplinary optimization of an electric aircraft for on-demand mobility," *2018 AIAA/ASCE/AHS/ASC Structures, Structural Dynamics, and Materials Conference*, 2018, p. 1384.

[3] Gur, O., "Maximum Propeller Efficiency Estimation," *Journal of Aircraft*, Vol. 51, No. 6, 2014, pp. 2035–2038. https://doi.org/10.2514/1.C032557, URL https://doi.org/10.2514/1.C032557.

[4] Gur, O., and Rosen, A., "Propeller performance at low advance ratio," *Journal of aircraft*, Vol. 42, No. 2, 2005, pp. 435–441.

[5] Gur, O., and Rosen, A., "Comparison between blade-element models of propellers," *The Aeronautical Journal*, Vol. 112, No. 1138, 2008, pp. 689–704.

[6] Rosen, A., and Gur, O., "A novel approach to actuator disk modeling," 2006.

[7] Madsen, H. A., Bak, C., Døssing, M., Mikkelsen, R., and Øye, S., "Validation and modification of the blade element momentum theory based on comparisons with actuator disc simulations," *Wind Energy: An International Journal for Progress and Applications in Wind Power Conversion Technology*, Vol. 13, No. 4, 2010, pp. 373–389.

[8] Madsen, H. A., Mikkelsen, R., Øye, S., Bak, C., and Johansen, J., "A Detailed investigation of the Blade Element Momentum (BEM) model based on analytical and numerical results and proposal for modifications of the BEM model," *Journal of Physics: Conference Series*, Vol. 75, IOP Publishing, 2007, p. 012016.

[9] Ning, A., Hayman, G., Damiani, R., and Jonkman, J. M., "Development and validation of a new blade element momentum skewed-wake model within AeroDyn," *33rd Wind Energy Symposium*, 2015, p. 0215.

[10] Mahmuddin, F., "Rotor blade performance analysis with blade element momentum theory," *Energy Procedia*, Vol. 105, 2017, pp. 1123–1129.

[11] Winarto, H., "BEMT algorithm for the prediction of the performance of arbitrary propellers," *Melbourne: The Sir Lawrence Wackett Centre for Aerospace Design Technology, Royal Melbourne Institute of Technology*, 2004.

[12] Gur, O., "Extending Blade-Element Model to Contra-Rotating Configuration," *IOP Conference Series: Materials Science and Engineering*, Vol. 638, IOP Publishing, 2019, p. 012001.

[13] MacNeill, R., and Verstraete, D., "Blade element momentum theory extended to model low Reynolds number propeller performance," *The Aeronautical Journal*, Vol. 121, No. 1240, 2017, pp. 835–857.

[14] Bontempo, R., and Manna, M., "Verification of the Axial Momentum Theory for Propellers with a Uniform Load Distribution," *International Journal of Turbomachinery, Propulsion and Power*, Vol. 4, No. 2, 2019, p. 8.

[15] Bontempo, R., and Manna, M., "Analysis and Evaluation of the Momentum Theory Errors as Applied to Propellers," *AIAA Journal*, Vol. 54, No. 12, 2016, pp. 3840–3848. https://doi.org/10.2514/1.J055131, URL https://doi.org/10.2514/1.J055131.

[16] Whitmore, S. A., and Merrill, R. S., "Nonlinear large angle solutions of the blade element momentum theory propeller equations," *Journal of aircraft*, Vol. 49, No. 4, 2012, pp. 1126–1134.

[17] Rwigema, M. K., "Propeller blade element momentum theory with vortex wake deflection," *27th International congress of the aeronautical sciences*, Vol. 2010, 2010, pp. 2–3.

[18] McCrink, M., and Gregory, J. W., "Blade element momentum modeling of low-Re small UAS electric propulsion systems," *33rd AIAA Applied Aerodynamics Conference*, 2015, p. 3296.

[19] Branlard, E., and Gaunaa, M., "Development of new tip-loss corrections based on vortex theory and vortex methods," *Journal of Physics: Conference Series*, Vol. 555, IOP Publishing, 2014, p. 012012.

[20] Shen, W. Z., Sørensen, J. N., and Mikkelsen, R., "Tip loss correction for actuator/Navier–Stokes computations," *J. Sol. Energy Eng.*, Vol. 127, No. 2, 2005, pp. 209–213.

[21] Shen, W. Z., Mikkelsen, R., Sørensen, J. N., and Bak, C., "Tip loss corrections for wind turbine computations," *Wind Energy: An International Journal for Progress and Applications in Wind Power Conversion Technology*, Vol. 8, No. 4, 2005, pp. 457–475.

[22] Sriti, M., et al., "Tip loss factor effects on aerodynamic performances of horizontal Axis wind turbine," *Energy Procedia*, Vol. 118, 2017, pp. 136–140.

[23] Glauert, H., "Airplane propellers," *Aerodynamic theory*, Springer, 1935, pp. 169–360.

[24] Bontempo, R., and Manna, M., "Effects of the approximations embodied in the momentum theory as applied to the nrel phase vi wind turbine," *International Journal of Turbomachinery, Propulsion and Power*, Vol. 2, No. 2, 2017, p. 9.

[25] Bontempo, R., and Manna, M., "Highly accurate error estimate of the momentum theory as applied to wind turbines," *Wind Energy*, Vol. 20, No. 8, 2017, pp. 1405–1419.

[26] Hwang, J. T., and Martins, J. R., "A fast-prediction surrogate model for large datasets," *Aerospace Science and Technology*, Vol. 75, 2018, pp. 74–87.

[27] Bouhlel, M. A., Hwang, J. T., Bartoli, N., Lafage, R., Morlier, J., and Martins, J. R. R. A., "A Python surrogate modeling framework with derivatives," *Advances in Engineering Software*, 2019, p. 102662. https://doi.org/https://doi.org/10.1016/j.advengsoft.2019.03.005.

[28] Drela, M., "XFOIL: An analysis and design system for low Reynolds number airfoils," *Low Reynolds number aerodynamics*, Springer, 1989, pp. 1–12.

[29] Mahmuddin, F., Klara, S., Sitepu, H., and Hariyanto, S., “Airfoil lift and drag extrapolation with viterna and montgomerie methods,” *Energy Procedia*, Vol. 105, 2017, pp. 811–816.

[30] Ning, S. A., “A simple solution method for the blade element momentum equations with guaranteed convergence,” *Wind Energy*, Vol. 17, No. 9, 2014, pp. 1327–1345.

[31] Ning, A., “Using blade element momentum methods with gradient-based design optimization,” *Structural and Multidisciplinary Optimization*, 2021, pp. 1–24.

[32] Brandt, J., and Selig, M., “Propeller performance data at low reynolds numbers,” *49th AIAA Aerospace Sciences Meeting including the New Horizons Forum and Aerospace Exposition*, 2011, p. 1255.

[33] Babuska, I., and Oden, J. T., “Verification and validation in computational engineering and science: basic concepts,” *Computer methods in applied mechanics and engineering*, Vol. 193, No. 36, 2004, pp. 4057–4066.

[34] Gill, P. E., Murray, W., and Saunders, M. A., “SNOPT: An SQP algorithm for large-scale constrained optimization,” *SIAM review*, Vol. 47, No. 1, 2005, pp. 99–131.

[35] Polaczyk, N., Trombino, E., Wei, P., and Mitici, M., “A review of current technology and research in urban on-demand air mobility applications,” *8th Biennial Autonomous VTOL Technical Meeting and 6th Annual Electric VTOL Symposium*, 2019.

[36] Chauhan, S. S., and Martins, J. R., “Tilt-wing eVTOL takeoff trajectory optimization,” *Journal of Aircraft*, Vol. 57, No. 1, 2020, pp. 93–112.